Materials Horizons

ROYAL SOCIETY OF CHEMISTRY

COMMUNICATION

View Article Online
View Journal | View Issue

Cite this: *Mater. Horiz.*, 2023, **10**, 5597

Received 22nd July 2023,
Accepted 22nd September 2023

DOI: 10.1039/d3mh01148h

rsc.li/materials-horizons

Pulsed laser welding of macroscopic 3D graphene materials†

Wenjie Yu,[ab] Weiwei Zhao[a] and Xiaoqing Liu *[a]

Welding is a key missing manufacturing technique in graphene science. Due to the infusibility and insolubility, reliable welding of macroscopic graphene materials is impossible using current diffusion-bonding methods. This work reports a pulsed laser welding (PLW) strategy allowing for directly and rapidly joining macroscopic 3D porous graphene materials under ambient conditions. Central to the concept is introducing a laser-induced graphene solder converted from a designed unique precursor to promote joining. The solder shows an electrical conductivity of 6700 S m^{-1} and a mechanical strength of 7.3 MPa, over those of most previously reported porous graphene materials. Additionally, the PLW technique enables the formation of high-quality welded junctions, ensuring the structural integrity of weldments. The welding mechanism is further revealed, and two types of connections exist between solder and base structures, *i.e.*, intermolecular force and covalent bonding. Finally, an array of complex 3D graphene architectures, including lateral heterostructures, Janus structures, and 3D patterned geometries, are fabricated through material joining, highlighting the potential of PLW to be a versatile approach for multi-level assembly and heterogeneous integration. This work brings graphene into the laser welding club and paves the way for the future exploration of the exciting opportunities inherent in material integration and repair.

New concepts

So far, no feasible strategy has been capable of welding macroscopic 3D graphene materials due to their inherent infusibility and insolubility. This work presents a pioneering welding conception of graphene, referred to as pulsed laser welding (PLW), which allows for rapidly joining 3D porous graphene materials. PLW offers not only powerful capabilities in the repair of local defects of graphene materials, but also direct access to novel 3D graphene architectural designs. Through joining of materials, PLW enables the construction of complex and multi-level graphene architectures that are fundamentally unattainable by traditional manufacturing means. Moreover, the PLW process eliminates the need for inert gas protection and complicated post-treatment, showing significant advantages in simplicity. This work opens a new avenue for 3D graphene materials design and construction, which is expected to draw substantial research interest in graphene science due to its versatility and flexibility in the process and its unprecedented capabilities in material integration.

Introduction

Throughout history, new manufacturing methods have been the foundation of the rapid development of graphene materials.[1] The early-stage progress in graphene manufacturing was traditionally made in response to the need for high-quality graphene at low cost, from mechanical exfoliation to Hummers' method (or variants thereof) to chemical vapor deposition and pyrolysis, shifting the material from the lab to real-world applications.[2] Under the prevailing trend of high performance and multifunctionality in various application areas, the strategies for tailoring graphene materials in terms of composition, morphology, and 3D architecture are in increasing demand.[3,4] Currently, while the methods for graphene chemistry and microstructure regulation have been considerably expanded, advances in 3D graphene engineering remain slow.[5,6] The established methods for fabricating 3D graphene include template-directed growth,[7] assembly,[8] and 3D printing.[9] However, none of them is unrestricted: some are in complex processes, some are in term of flexibility, and some are in terms of throughput/efficiency. Moreover, all these methods have limited capabilities in regulating the structural and compositional complexity. The realization of these challenges will constitute the next higher level of graphene manufacturing.

[a] *Key Laboratory of Marine Materials and Related Technologies, Ningbo Institute of Materials Technology and Engineering, Chinese Academy of Sciences, Ningbo, 315201, China. E-mail: liuxq@nimte.ac.cn*

[b] *University of Chinese Academy of Sciences, Beijing, 100049, China*

† Electronic supplementary information (ESI) available: Characterization of synthesized precursors; Raman and XPS analysis, XRD pattern, and SEM and TEM images; tensile stress–strain curve; EDS, *I–V* curves, and EMI SE results. See DOI: https://doi.org/10.1039/d3mh01148h

Among the various advanced manufacturing technologies, welding possesses particular advantages of simple operation, versatility, and flexibility, and has thereby been an irreplaceable part of modern manufacturing.[10] Not surprisingly, there have been long efforts to diversify weldable materials, starting with metals, then including woods,[11] ceramics,[12] polymers,[13] and, more recently, MXene.[14] These pioneering works have convincingly demonstrated the promise of welding, where architectures with unprecedented complexity and functionality could be readily shaped by material joining. Consequently, developing a graphene welding technique should be an indispensable step for addressing the diversity gap of graphene manufacturing and holds enormous untapped potential for materials discovery and optimization. However, graphene materials can neither be melted, nor sintered, nor polymerized, which poses several obstacles in joining graphene materials. Current welding mechanisms are based on material diffusion bonding and are therefore specific to the meltable or soluble materials. A new advanced welding strategy available for macroscopic graphene materials will be a significant complement to welding theories.

In this study, we conceptually develop and experimentally demonstrate a pulsed laser welding (PLW) technique capable of directly joining macroscopic 3D porous graphene materials under ambient conditions. The key idea involves the introduction of a high-quality laser-induced graphene (LIG) solder which was converted from an organic precursor with well-designed rheological properties using 10.6 μm pulsed laser irradiation. Simultaneously with the laser conversion, the base graphene structures were welded. The overall welding process combines laser processing and material joining in an integrated approach, with consequent merits of rapidity, scalability, and low energy consumption. More importantly, owing to the powerful capabilities in materials integration, PLW can offer vast flexibility in graphene architectural design beyond the limits of traditional manufacturing means. In addition to the emerging 3D geometries like the hollow cylinder and Möbius strip, more complex architectural designs are also allowed to be accessed *via* PLW. This welding conception provides a powerful platform to broaden the possibility of architectural designs of graphene.

Results and discussion

Design rationale of a pulsed laser welding (PLW) technique

As shown in Fig. 1a, the PLW process involved two simple steps. First, an organic compound was introduced as an adhesive precursor to pre-connect base graphene materials. Then, the precursor was directly converted into an LIG solder by 10.6 μm pulsed laser irradiating. The graphene materials were integrated *via* the welded junction, which was fused by base structures and formed an LIG solder. Notably, the free-standing porous graphene films were chosen as the base materials for the demonstration of PLW because of their high universality in applications. On the other hand, porous films have arguably been the most popular, varied, and accessible graphene architectures, and their production and modification have matured over the past decade.[4]

Obviously, the adhesive precursor must fulfill two basic requirements to guarantee the feasibility of PLW: (i) the

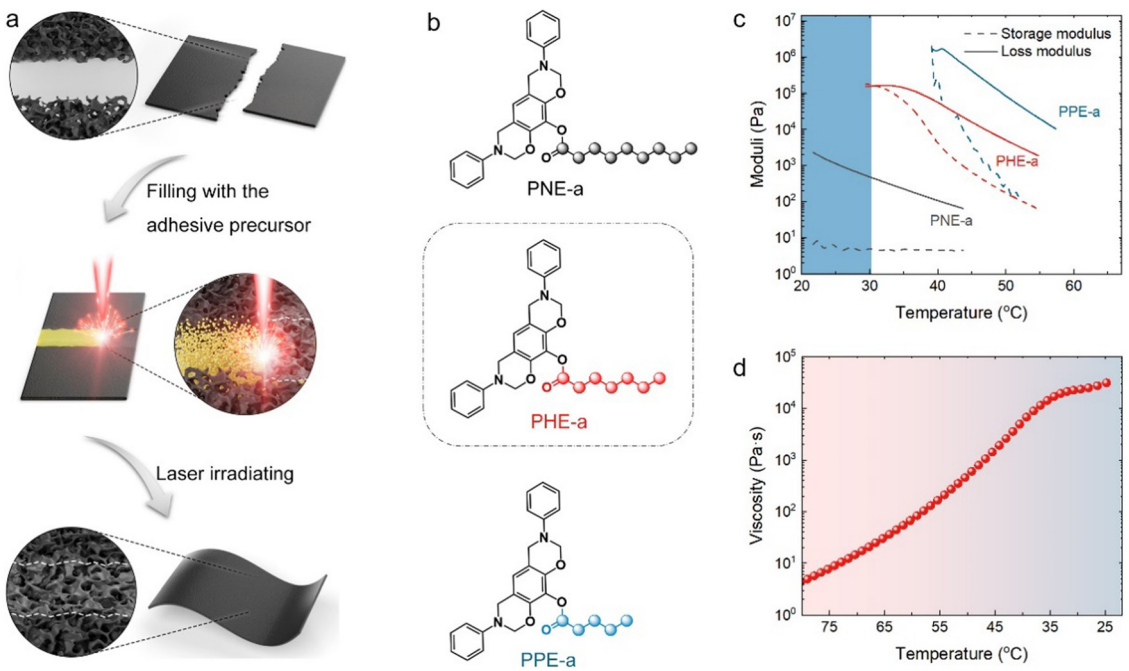

Fig. 1 Molecular design of organic adhesive precursors. (a) Schematic illustration of the PLW process for porous graphene film materials. (b) Molecular structures of three synthesized candidate adhesive precursors. (c) Storage and loss modulus as a function of temperature of PNE-a, PHE-a, and PPE-a. The blue area represents the room temperature range. (d) The evolution of apparent viscosity of PHE-a in the temperature range of 25–80 °C.

precursor allows to be directly converted into a high-quality LIG solder without the need for catalysts and the protection of inert gas, and, most importantly, (ii) it can fully come into contact with the base graphene structures, so that formed LIG solder structures achieve perfect integration and seamless connectivity with base structures. The first challenge for this laser welding technique is to develop a proper precursor since none of the reported carbon sources for laser-induced graphitization could perfectly meet the requirements. Specifically, the existing precursors are largely limited to solids with defined physical geometry and infusible molecular structure (graphene oxide (GO), polyimide, polybenzimidazole, polyether ether ketone, and cross-linked polystyrene).[15] The intimate contact of solid precursors with the base graphene structures is a big problem. Even if they exist in the powder form, the voids are unavoidable in solid contact. Owing to the inherently high fluidity, gaseous precursors (*e.g.*, CH_4) can easily pervade the base structures.[16] However, the gas-based graphene formation relies critically on the catalytic effect of metal substrates and is almost prohibitively time-consuming and scenario-limited. Although liquids are technically promising for PLW, they cannot be spatially confined under capillary forces and gravity, implying unexpected materials diffusion and runoff when welding porous and unclosed structures.[17]

Herein, the solution is inspired by the gelation strategy, which has fundamentally been a technical core of nozzle-based 3D printing where the ink material can convert from a liquid to gel after deposition to retain its shape.[9] In this work, the adhesive precursor was designed to gel through temperature changes, a mild and reversible process. Ideally, it was a liquid above room temperature (RT, 25 ± 5 °C) for reliable flow. Once injected between the two base materials, the precursor evolved into a shape-fixed gel as it gradually cooled to RT, preventing its random flow and bonding them together. The temperature decrease was caused by the spontaneous heat exchange between the precursor and the environment. The duration of material cooling was thus allowed to be tuned by altering its initial temperature. To achieve this, we designed and synthesized a set of organic precursor candidates (Fig. S1, ESI†). As shown in Fig. 1b, three precursors, named PPE-a, PHE-a, and PNE-a, were synthesized by combining the same benzoxazine structure with pentanoyl, heptanoyl, and nonanoyl groups, respectively. The oxazine structure was designed for the highly efficient flame retardancy of precursors, which was crucial for preventing their direct ablation and facilitating graphitization. The alkyl chain was introduced to adjust the molecular flexibility.[18]

As shown in Fig. 1c, the storage modulus of PNE-a remained almost constant with decreasing temperature, suggesting its liquid form at RT and above. As a result of the shortened flexible chain, the storage modulus of PHE-a dramatically increased with decreasing temperature and finally intersected with its loss modulus at ~32 °C. This indicated the occurrence of a gelation transformation: PHE-a existed in the liquid form until the operating temperature dropped below 32 °C and then evolved into a gel in the semisolid state.[9] Likewise, the gelation temperature of PPE-a with the shorter flexible chain was found to be ~39 °C. In view of the results of rheological properties, both PHE-a and PPE-a could be melted into the liquid with high fluidity and form a gel upon cooling and are thus applicable for PLW. Considering that PHE-a had a lower gelation temperature close to RT, which was beneficial to practical operation, it was preferably used as the adhesive precursor for PLW.

The thermal properties of PHE-a were further investigated by viscosity and differential scanning calorimetry (DSC) measurements. The apparent viscosity *versus* temperature showed that the precursor fluidity could be tuned in real-time through temperature control (Fig. 1d). The higher initial temperature would lead to a lower viscosity, which favored the precursor diffusion in base materials. In addition, the viscosity increased exponentially with the decreasing temperature and finally stabilized at a superelevated value of 10^4–10^5 Pa s when the temperature was <34 °C. This agreed well with the moduli analysis. The DSC results further revealed a frozen molecular configuration of PHE-a at a temperature below 11.5 °C (Fig. S2, ESI†). Most significantly, the contact angle (CA) between liquid PHE-a (at the temperature of 90 °C) and graphene film was measured to be 25.3° (Fig. S3, ESI†). The precursor was shown to have a strong affinity for graphene, probably arising from their π–π interactions.[19] This ensured that the liquid adhesive precursor could spontaneously infiltrate with the base graphene structure under interfacial tensions.

Structural and property analysis of an LIG solder

As expected, PHE-a could be directly converted into high-quality LIG structures by 10.6 μm pulsed laser irradiation. X-ray photoelectron spectroscopy (XPS) analysis showed that the laser-induced product had a high carbon content of 95.7% (Fig. S4, ESI†), far exceeding the theoretical carbon content of 82.8% of PHE-a. Under laser irradiation, the non-carbon elements in precursors would mostly recombine into gaseous products and released rapidly. On the other hand, this resulted in a run-through-macropore network structure as captured by scanning electron microscopy (SEM) (Fig. S5, ESI†). The low oxidation (4.3% O) of the product was also likely attributed to the release of large quantities of gases that diluted the oxygen content in the local air space and thus prevented the oxidation of materials. The high-resolution C 1s spectrum further revealed that most carbon atoms were bonded with sp^2 structures, reaching 66% (Fig. 2a), higher than the thermal-reduced graphene oxide.[20] The high content of sp^2 C pointed to the formed graphene structure as identified by Raman spectra (Fig. 2b). As shown, three characteristic peaks for graphene located at 1351, 1585, and 2698 cm^{-1} were detected and assigned to D, G, and 2D peaks, respectively.[21] The sharp G peak had a full width at half maximum (FWHM) of 44 cm^{-1} (Fig. S6, ESI†), indicating a high graphitization level. Moreover, the 2D peak was fitted as a single Lorentzian peak with a large FWHM of 64 cm^{-1} (Fig. S7, ESI†). This was characteristic of graphene materials consisting of randomly stacked graphene layers along the *c* axis.[22]

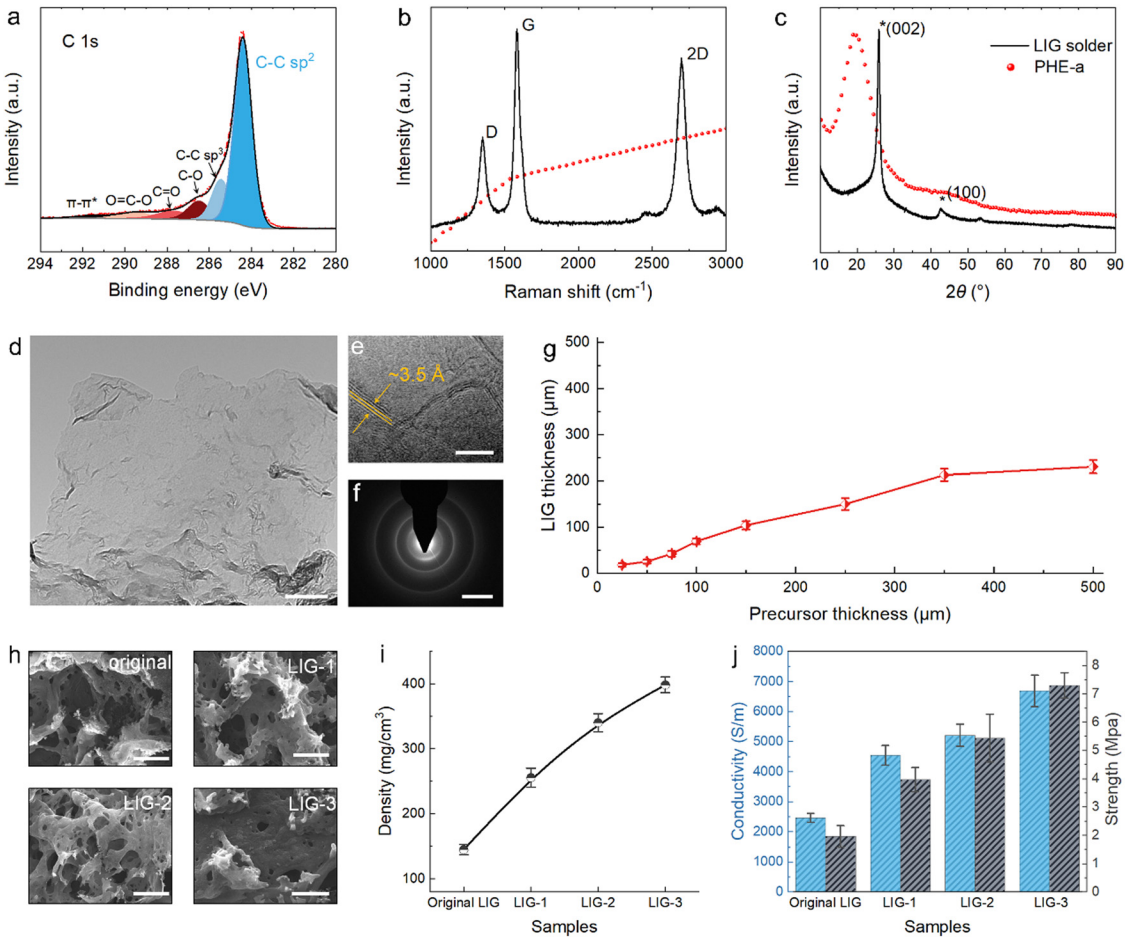

Fig. 2 Characterization of the LIG solder structure. (a) High resolution XPS C 1s spectrum of the LIG solder. (b) Raman spectra and (c) XRD patterns of the LIG solder and PHE-a. (d) A TEM image taken at the edge of LIG flakes; the scale bar is 0.1 μm. (e) The wrinkled nanostructures of LIG solder; the scale bar is 5 nm. (f) SAED pattern derived from d); the scale bar is 5 nm. (g) Correlation of solder thickness with the precursor thickness. (h) SEM images of LIG solders that underwent different times of precursor infiltration and pyrolysis; the scale bars are 20 μm. (i) Density of original LIG, LIG-1, LIG-2, and LIG-3. (j) Electrical conductivity and mechanical strength of different solder samples.

The multilayered structure of LIG solder was indeed confirmed by the X-ray diffraction (XRD) pattern, where a pronounced (002) peak centered at a diffraction angle $2\theta = 26.0^\circ$ could be found (Fig. 2c). Accordingly, the interlayer spacing was calculated to be ~3.4 Å using the Bragg equation. Transmission electron microscopy (TEM) was employed to characterize the nanostructure of the solder, and the large-size graphene flake transparent to the electron beam could be directly observed (Fig. 2d). Moreover, from the high-resolution TEM image, the average thickness of graphene flakes was estimated to be 3–4 atomic layers, with an average interlayer space of ~3.5 Å, agreeing well with the XRD results (Fig. S8, ESI†). In addition, wrinkled nanostructures were also found on the surface of LIG solder flakes (Fig. 2e). The wrinkled feature and the expanded interlayer space could result from the instantaneous heating process and rapid release of gaseous products.[23] Finally, the electron diffraction pattern showed a polycrystalline graphene structure of the LIG solder (Fig. 2f).[24]

We further summarized the correlation between the precursor thickness and LIG solder thickness, aiming to provide a reference for the practical welding experiment (Fig. 2g). The LIG solder thickness was relatively easy to adjust by varying the precursor thickness. In addition, based on the fusibility of the adhesive precursor, we demonstrated an effective way to regulate the structures and properties of the LIG solder, namely, precursor infiltration and pyrolysis – injecting the molten precursor into the LIG solder skeleton and conducting laser irradiation again. The solder that underwent the infiltration and pyrolysis treatment was designated as LIG-X, where "X" stood for the cycle of treatment. As shown in Fig. S9 (ESI†), the thickness of the solder structure was slightly increased after the multiple treatments. The morphology and Raman analysis further suggested that both density and quality of the solder were improved after the precursor infiltration and pyrolysis (Fig. 2h and Fig S10, ESI†). For example, after one, two, and three cycles of precursor infiltration and pyrolysis, the density of the LIG solder increased from the original 140 mg cm^{-3} to 260 mg cm^{-3}, 340 mg cm^{-3}, and 400 mg cm^{-3}, respectively (Fig. 2i). Moreover, LIG-3 possessed a conductivity of 6700 S m^{-1} and tensile strength of 7.3 MPa, which were

~270% and 720% of the original value, respectively (Fig. 2j and Fig. S11, ESI†). Notably, such performance has already exceeded that of most previously reported porous graphene films (Fig. S12, ESI†). Overall, with the strategy of precursor infiltration and pyrolysis, the properties of LIG solder could be flexibly adjusted to match the base material, preventing the welded part from becoming the weak part of the weldment.

Welding of porous graphene films

The confirmation of the feasibility of the PLW concept started with the design of butt joint welding experiments for investigating two key properties of resultant weldments: (i) mechanical strength, which was responsible for the stability and durability of welded structures in the application, and (ii) electrical conductivity, which distinguished PLW from traditional glue bonding. The rectangular welding base materials with the same size were cut from a free-standing porous graphene film which was produced following the reported research[25] and had a thickness of 40 μm, a tensile strength of 2.73 MPa, and a conductivity of 6600 S m^{-1}. The series-connected welding structure was adopted for the purpose of maximizing the impact of solder properties on weldments.

In the tensile test, the direction of applied force was perpendicular to the weld, and the mechanical strength theoretically followed the Cannikin law, dependent on the sample's weakest part. Hence, based on the location of the tensile failure, it could be inferred whether the solder robustly connected two individual components. Fig. 3a shows two kinds of solders with different strengths for welding: the original LIG solder of 1.96 MPa strength (case A) and LIG-1 of 3.97 MPa strength (case B). During the PLW process, the precursor thickness was controlled to match the solder and base structure in terms of thickness (details are provided in the Methods section), and a large weld width of ~6 mm was set to facilitate the identification of the break location after the tensile test. In case A, the average tensile strength of weldment was measured to be 1.89 MPa, and the failure occurred in the solder, which was caused by the lower strength of the solder than the base

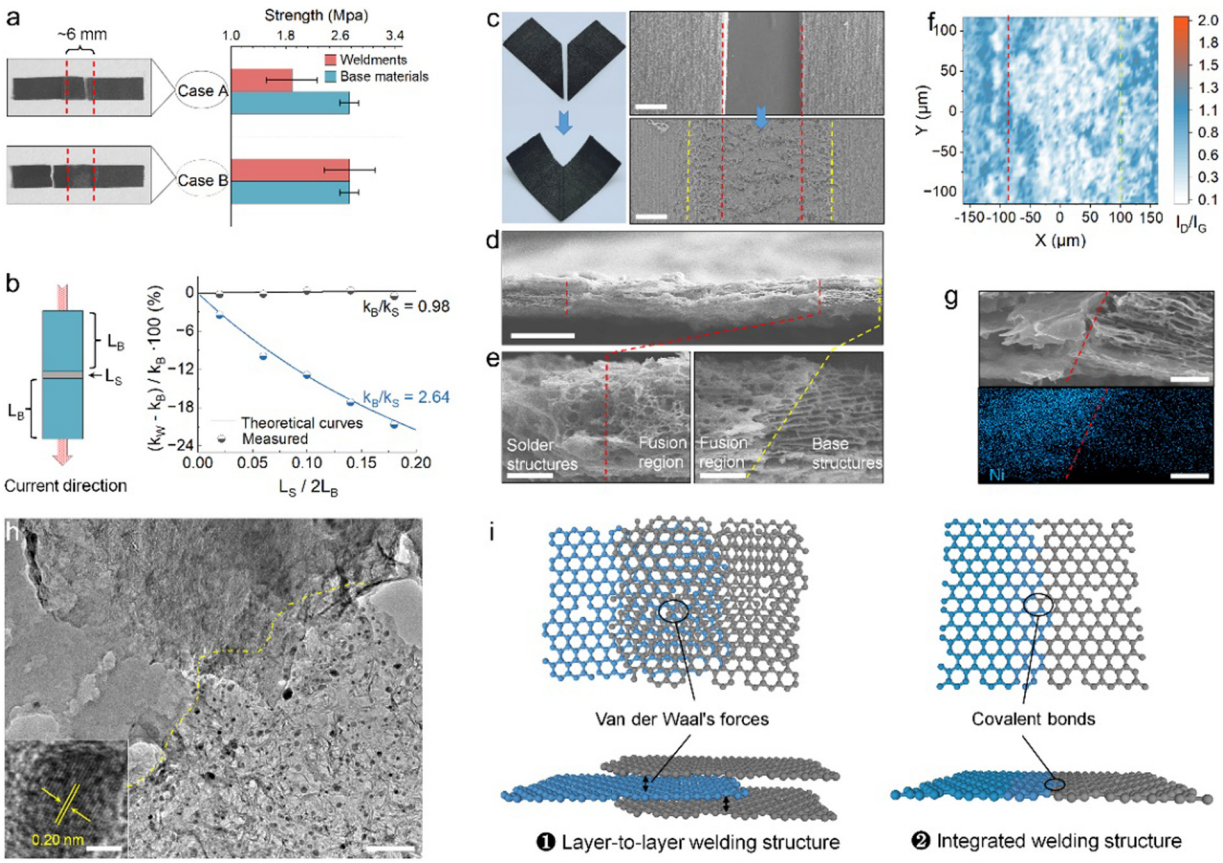

Fig. 3 Analysis of the structure and performance of graphene weldments. (a) Mechanical properties of two weldments that were welded by solders with different strengths. (b) Electrical conductivity loss of weldments compared to the base material and its dependence on the weldment width. (c) Digital and SEM images of graphene films before and after PLW; the scale bar is 200 μm. The red dashed lines are used to distinguish the solder structures and fusion structures, and the yellow dashed lines are used to distinguish the base structures and fusion structures. (d) Cross-section SEM view of the weldment; the scale bar is 100 μm. (e) The high-resolution cross-section views taken at the fusion region of the solder and the base material; the scale bars are 20 μm. (f) Raman I_D/I_G mapping image of the junction part. (g) Cross-section SEM image and corresponding EDS mapping of the junction part of Ni-solder and base structures; the scale bars are 5 μm. (h) TEM image of the fusion region of the Ni-solder and base graphene structure; the scale bar is 100 nm. Inset is a high-resolution TEM image of a Ni nanoparticle, showing a lattice spacing of 0.20 nm; the scale bar is 2 nm. (i) Illustration of two types of connections between the solder and base structures. Blue: base graphene structures. Grey: LIG solder structures.

material while in the case B, the weldment was fabricated with a stronger solder, and the fracture took place in the base material. The tensile strength close to that of the base material was thus measured, reaching 2.72 MPa. Notably, in both welding cases, the welded junctions remained intact after the test. This suggested that the strength of the welded junction was superior to that of the solder and base materials.

Furthermore, the electrical performance of the weldment was evaluated with the method of Volt-Ampere, in which the current and the weld were also mutually perpendicular. Theoretically, if the LIG solder is well fused and connected to the base materials forming robust and conductive graphene junctions, then

$$R_W = 2R_B + R_S \quad (1)$$

where R_W, R_B, and R_S are the resistance of the weldment, base materials, and the solder, respectively. We note that the resistance, R, can be calculated by $R = L/(k{\cdot}S)$, where L, k, and S are the length, conductivity, and cross-sectional area of the material, respectively. Substituting this in the above and assuming that the weldment has a uniform cross-sectional size, we get

$$(k_w - k_B)/k_B = (1 - k_B/k_S)/(2L_B/L_S + k_B/k_S) \quad (2)$$

where k_B, k_S, and k_W denote the conductivity of base materials, the solder structure, and the weldment, respectively, L_B denotes the length of the base material, and L_S denotes the weld width. Evidently, relative to the mechanical strength of weldments, the apparent conductivity is affected by more factors, including not just the joining quality and the conductivity of the solder and the base material, but the weld width. To verify this, two groups of experiments were performed where the base materials were respectively welded with original LIG solder (k_B/k_S = 2.64) and LIG-3 (k_B/k_S = 0.98), and the weld width was taken as the variable. As shown in Fig. 3b, the experimental values coincided well with the theoretical curves plotted based on the eqn (2). This result practically indicated two noteworthy aspects. First and foremost, PLW enabled the formation of a highly conductive junction between the solder and base structures. The slight deviation from the theoretical forecast was likely caused by the presence of connection defects and contact resistance. Secondly, with sufficiently narrow weld widths, the relative conductivity loss of the weldment could be reduced to a negligible level even if the conductivity of the solder was much lower than that of the base materials. For instance, in the case of k_B/k_S = 2.64, the apparent conductivity of the resultant weldment was only $<$10.0% lower than that of the base material as long as the weld width was controlled to $<$7.3% of the base material size ($2L_B$).

The origin of high mechanical robustness and electrical conductivity of welded junctions was revealed through the structural analysis of weldments. As shown, no obvious welding defects were observed from digital and SEM images (Fig. 3c and d). From high-resolution cross-section SEM views (Fig. 3e), a region distinct from the solder and the base material could be clearly identified. This region was attributed to the fusion of the base material with the solder transformed from the infiltrated adhesive precursor; thus, it showed a denser and mechanical interlock structure. Raman mapping images further indicated a higher graphitization degree of the fusion structure (Fig. S13, ESI†). Generally, a larger I_D/I_G ratio signifies a greater degree of disorder in the structures. As shown in Fig. 3f, the I_D/I_G ratio of the solder and base structure approximately ranged from 0.3 to 0.6, while the I_D/I_G ratio of the fusion region was found to be lower at 0.2–0.4. This distinction was largely attributed to the graphene structure-directing effect – the base graphene structure served as a template to catalyze the conversion of high-quality laser-induced structures from pre-fused adhesive precursors under laser irradiation.[26] Altogether, the denser, high-quality, and highly integrated fusion structure was responsible for the impressive physical performance of the welded junction.

Of note, due to the fact that the fused solder and the base material were graphene materials with very similar sheet-like nano-features, it was hard to detail the connection by distinguishing one from another. To address this, a Ni nanoparticle-containing solder (Ni-solder) was adopted to form a heterogeneous junction for further uncovering the joining mechanism between the solder and base materials. The Ni-solder was introduced using a mixture of PHE-a and nickel acetylacetone as the adhesive precursor. XRD result confirmed the nanocrystal structure of Ni nanoparticles, and their even distribution in the solder was characterized by TEM (Fig. S14, ESI†). The uniform distribution of small-size Ni nanoparticles could be attributed to the fast nucleation kinetics at laser-induced high temperature and the ultrafast laser heating process that limits the aggregation and growth of the particles.[27,28] Due to the difference in the Ni content, the solder structure and fusion structure could be visually distinguished by SEM-EDS (Fig. 3g). Moreover, the connection details of the two could be clarified through the high-resolution TEM image of the fusion region (Fig. 3h). As shown, the solder structure contained abundant Ni nanoparticles uniformly and densely decorated on the solder flake, while the base structure was composed of only thin graphene sheets. Consequently, a fine dividing line between the solder and base structures could be identified based on the distribution feature of Ni nanoparticles. Interestingly, some parts of the fusion region were found to show overlapped nanostructures, where solder flakes were overlaid on the base structure. In addition, the continuous graphene flake with both the solder and base structures could also be observed (Fig. S15, ESI†). As such, we proposed that the PLW had enabled the formation of two types of connection between the solder and base materials (Fig. 3i): (i) Layer-to-layer welding structures, in which graphene sheets of solder and base material were connected *via* intermolecular forces; (ii) integrated welding structure, in which the solder structures were covalently bonded to the base graphene.

Freeform graphene architectures constructed *via* PLW

Providing direct and rapid access to freeform architectures represents the core function of the welding technique. Rather than preparing graphene materials from GO or other specific hydrocarbons as in conventional manufacturing, the welding

approach focuses on rebuilding available graphene structures into architectures with desired structural features through material joining. PLW can therefore be regarded as a compatible platform that bridges the capability gap between existing graphene manufacturing methods to offer additional integrated options in the 3D design and construction of graphene materials. It is well known that graphene materials hybridized with different functional components (such as metals, semiconductors, organics, *etc.*) possess distinct physicochemical properties like absorbance, catalytic activity, and zeta potential.[6] Combining different characteristics into an integrated complex graphene system is technically compelling and has shown valuable in various applications.[29–34] For example, assembling carbon materials with opposite ion preferences into a single device has proven useful in hydro-voltaic technology.[35] In addition, integrating two graphene structures with distinct semi-conducting behavior (n-type doped and p-type doped) bears the potential to form graphene p–n junctions, the elementary entities for many electronic devices.[36] Consequently, the integration capability of PLW, which provides strong viability in multi-level assembly and heterogeneous integration, may spark enormous renewed interest in exploring the opportunities inherent in novel architectural designs and is expected to play an important role in the present and future research of graphene.

As a demonstration of PLW capabilities, we welded four graphene films hybridized with elements of Ni, Cr, Al, and Fe, respectively, into an integrated 2D puzzle (Fig. 4a). To the best of our knowledge, the fabrication of such a macro lateral graphene heterostructure has yet to be previously reported, which is ascribed mainly to the limited construction ability of traditional technologies. SEM views showed that the four graphene films were well connected by the LIG solder. EDS analysis further revealed that the four metal elements in the puzzle displayed the separable feature, where each functional region was connected and distinguished by the solder structure. Due to the customizable geometry and composition of LIG structure, the solder could also serve as a unique functional part of welded structures. As shown, a concentric pattern was fabricated using a graphene hollow ring as the base material and filling it with the N-doped solder (N-solder) transformed from the melamine-containing adhesive precursor. XPS analysis confirmed the ultra-high N-doping level in N-solder structures, reaching 13.4% (Fig. S16, ESI†). The N-solder was shown to be hydrophilic (CA = 73.5°) due to the N-doping effect, while the CA of the base structure was measured to be 152.2°. The sharp change in surface wettability led to a Moses effect on the surface of the weldment, where the water was resisted within the boundary of N-solder structures.

PLW also offered a high degree of flexibility for designing vertical heterostructures of graphene materials. One way was called ''lap welding,'' where the solder integrated two films. Two different graphene films were bonded face to face by the adhesive precursor. Then the upper surface was exposed to the laser irradiation to convert the precursor into the solder, integrating them into a Janus film (Fig. 4b). Because the underlying film was hydrophilic and the upper one was superhydrophobic (Fig. S17, ESI†), the welded Janus film displayed a self-floating performance on the water. Such Janus structures have drawn substantial interest in solar energy desalination and electrocatalysis.[37,38] SEM images clearly showed that the two graphene films were seamlessly integrated by the solder. It was worth noting that lap welding had rigid requirements on the structure of the upper film. One obvious requirement was the through-hole structure, providing the necessary channels facilitating the release of gas products. Besides, the thickness was preferably less than ~65 μm under our laser parameters so that the laser-induced heat was able to conduct into the precursor to drive its graphitization (Fig. S18, ESI†). Apparently, the critical thickness of the upper layer was related to the laser power, exposure time, and its thermal conductivity. Alternatively, the other strategy towards the vertical heterostructures was to utilize the LIG solder as the building block. Fig. S19 (ESI†) showed a three-layer graphene film fabricated by forming Ni-solder and Fe element nanoparticles-containing solder (Fe-solder) on a base film in sequence. SEM and EDS analysis confirmed their successful integration and revealed a hierarchic arrangement of chemical compositions.

What's more, the architectural design of graphene enabled by PLW was not limited to the planar structure; more complex 3D geometries were also allowed. To prove this, a hollow cylinder which has attracted much attention in water purification and desalination,[39] and a Möbius strip with a topologically four-dimensional structure,[40] were produced by joining two ends of the graphene film (Fig. 4c and Fig. S20, ESI†). Due to the high robustness of welded graphene junctions, these two welded shapes were stabilized despite the deformation pressure. Although it was technically possible for such complex structures to be fabricated *via* template-directed growth and advanced 3D-printing methods, they were time- and energy-consuming and had a high equipment requirement. The PLW inherited virtually all advantages of the lithography manufacturing technique and avoided the need for inert gas protection and complicated post-treatment, providing rapidity and simplicity. On the other hand, the wall thickness of the welded cylinder and Möbius strip was only ~40 μm and could be lowered by using thinner base graphene films. As a comparison, the critical resolution of 3D-printing structures was roughly 100 μm, which was limited by the diameter of GO-based filament.[41] This emphasized that the welding strategy outperformed conventional routes in terms of the preparation period/process and the structural resolution of products. Additionally, PLW was based on the planar graphene films as base materials, whose hybrid-composite design and hierarchical organization could be tailored on demand upon the strategy we introduced above. Therefore, the opportunity space provided by PLW, for example, towards producing spatially resolved 3D hetero-architectures and exploring related potential applications, shows no boundaries.

Apart from the ability for graphene architecture construction, the PLW could also repair macroscopic graphene materials and weld circuit boards. Due to the inherent brittleness of

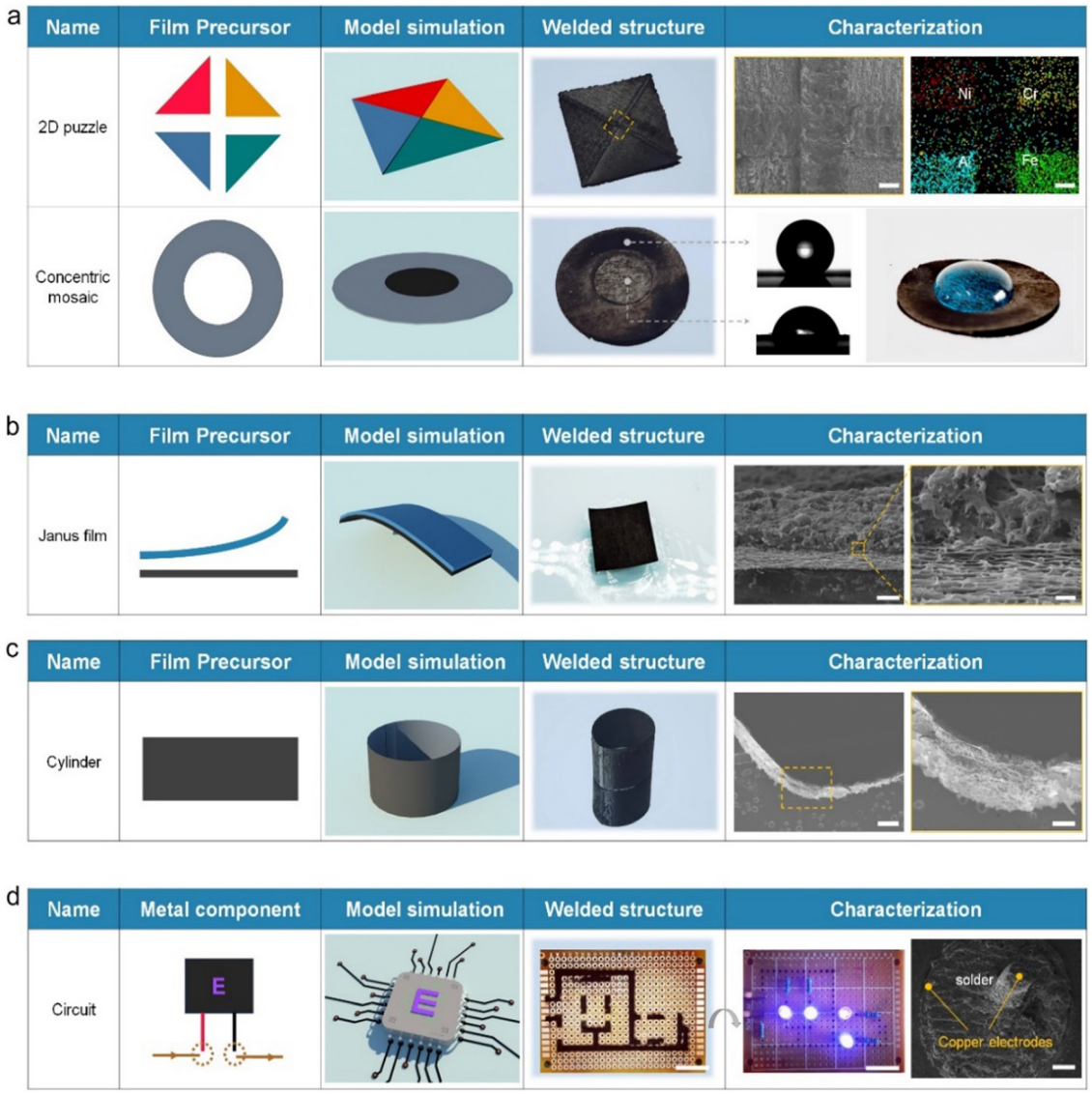

Fig. 4 Design and construction of various complex graphene architectures *via* PLW. (a) A 2D puzzle integrated with four disparate graphene films and a concentric mosaic produced from a graphene hollow ring using N-doped solder; corresponding digital images, SEM image, EDS result, and water contact angle; the scale bars are 400 μm. (b) A Janus film integrated with two films, each with distinct morphologies and surface wettability; a digital image of the Janus film on water; the corresponding SEM image and its enlarged version, the scales bars are 60 and 10 μm, respectively. (c) A graphene cylinder produced using a flexible graphene film as the base material; corresponding digital image; SEM image and its enlarged version, the scale bars are 500 and 200 μm, respectively. (d) A commercial printed circuit board with nine electronic components integrated by LIG solder; digital images of the front and reverse sides of the circuit, the scale bars are 10 mm; SEM image of metal–graphene junction, the scale bar is 300 μm.

carbon matter, graphene materials were generally prone to damage and could not be repaired until the PLW was developed. Fig. S21 (ESI†) showed that two typical macroscopic defects of graphene materials, including cracks and notches, could be repaired *via* PLW. *I–V* curves, electromagnetic interference shielding effectiveness (EMI SE) results, and SEM images suggested that the structure and properties of damaged graphene films were basically restored after the PLW process. To demonstrate the capacity of PLW in circuit board welding, we integrated nine electronic components on a commercial printed circuit board with the LIG solder (Fig. 4d). SEM images indicated that the solder was fully attached to the copper electrodes, forming an electrical pathway. As a result, light bulbs in the system worked stably with the applied voltage. However, frankly speaking, there is an evident performance gap between our porous graphene solder and conventional metallic solders (*e.g.*, tin) in terms of conductivity and strength. Moreover, due to the difference between Dirac-type carriers in graphene and the Schrodinger-type carriers in metals, the weld contact resistance of graphene solder is much higher than that of metallic solder.[42] Nonetheless, considering carbon materials have excellent acid and alkali resistance, corrosion resistance, thermostability, and chemical stability, the graphene solder afforded by PLW might be superior to the metallic solder for use in harsh environments.

Conclusions

We have developed a laser welding technique for macroscopic porous graphene materials. Porous graphene films as base materials were directly joined together under ambient conditions by introducing a laser-induced graphene solder converted from an adhesive precursor using pulsed laser irradiation. With a strategy of precursor infiltration and pyrolysis, the properties of the solder were tuned to match the base materials. Moreover, the welded junction showed well-preserved electrical conductivity and higher mechanical robustness compared to the solder and base structures. This mainly results from the denser and interlocked structures through intermolecular forces and covalent bonds in the fusion region of solder and base materials. Furthermore, the capabilities of PLW in 3D graphene engineering were demonstrated through fabricating the structures of technical challenges (*e.g.*, complex 3D geometries of a hollow cylinder and a Möbius strip, lateral/vertical heterogeneous structures). The manufacturing principle of PLW that takes the porous graphene film structures as building blocks opens enormous opportunities for designing graphene 3D architectures with apparently limitless combinations of spatially defined characteristics and functionalities. Besides, PLW could also be used to repair macroscopic graphene materials and weld circuit boards. We envision that these PLW capabilities provide versatile tools aiding material researchers in creating new graphene architectures and making more thoughtful use of materials.

Author contributions

W. Yu: methodology, investigation, writing – original draft. W. Zhao: analysis, writing – review & editing. X. Liu: supervision, conceptualization.

Conflicts of interest

The authors declare no competing interests.

Acknowledgements

The authors greatly acknowledge the financial support from National Natural Science Foundation of China (52003282 and U1909220), the Zhejiang Provincial Natural Science Foundation of China under Grant No LR20E030001, the Leading Innovative and Entrepreneur Team Introduction Program of Zhejiang (Grant No. 2021R01005), the Foundation of the Director of NIMTE (2022SZKY0311), and the National Ten Thousand Talent Program for Young Top-notch Talents, Ten Thousand Talent Program for Young Top-notch Talents of Zhejiang.

References

1 W. Kong, H. Kum, S. H. Bae, J. Shim, H. Kim, L. Kong, Y. Meng, K. Wang, C. Kim and J. Kim, *Nat. Nanotechnol.*, 2019, **14**, 927–938.
2 L. Lin, H. Peng and Z. Liu, *Nat. Mater.*, 2019, **18**, 520–524.
3 M. F. El-Kady, Y. Shao and R. B. Kaner, *Nat. Rev. Mater.*, 2016, **1**, 16033.
4 Z. Sun, S. Fang and Y. H. Hu, *Chem. Rev.*, 2020, **120**, 10336–10453.
5 X. Liu and L. Dai, *Nat. Rev. Mater.*, 2016, **1**, 16064.
6 D. Deng, K. S. Novoselov, Q. Fu, N. Zheng, Z. Tian and X. Bao, *Nat. Nanotechnol.*, 2016, **11**, 218–230.
7 X. F. Jiang, R. Li, M. Hu, Z. Hu, D. Golberg, Y. Bando and X. B. Wang, *Adv. Mater.*, 2019, **31**, 1901186.
8 P. He, T. Du, K. Zhao, J. Dong, Y. Liang and Q. Zhang, *Adv. Mater.*, 2023, **35**, 2208562.
9 C. Zhu, T. Y. Han, E. B. Duoss, A. M. Golobic, J. D. Kuntz, C. M. Spadaccini and M. A. Worsley, *Nat. Commun.*, 2015, **6**, 6962.
10 J. P. Oliveira, T. G. Santos and R. M. Miranda, *Prog. Mater. Sci.*, 2020, **107**, 100590.
11 B. Gfeller, M. Zanetti, M. Properzi, A. Pizzi, F. Pichelin, M. Lehmann and L. Delmotte, *J. Adhes. Sci. Technol.*, 2003, **17**, 1573–1589.
12 E. H. Penilla, L. F. Devia-Cruz, A. T. Wieg, P. Martinez-Torres, N. Cuando-Espitia, P. Sellappan, Y. Kodera, G. Aguilar and J. E. Garay, *Science*, 2019, **365**, 803–808.
13 M. B. Gordon, J. M. French, N. J. Wagner and C. J. Kloxin, *Adv. Mater.*, 2015, **27**, 8007–8010.
14 J. Wang, Y. Liu, Y. Yang, J. Wang, H. Kang, H. Yang, D. Zhang, Z. Cheng, Z. Xie, H. Tan and Z. Fan, *Matter*, 2022, **5**, 1042–1055.
15 Y. Chyan, R. Ye, Y. Li, S. P. Singh, C. J. Arnusch and J. M. Tour, *ACS Nano*, 2018, **12**, 2176–2183.
16 J. B. Park, W. Xiong, Y. Gao, M. Qian, Z. Q. Xie, M. Mitchell, Y. S. Zhou, G. H. Han, L. Jiang and Y. F. Lu, *Appl. Phys. Lett.*, 2011, **98**, 123109.
17 W. Yu, W. Zhao, S. Wang, Q. Chen and X. Liu, *Adv. Mater.*, 2023, **35**, 2209545.
18 J. Liu, S. Wang, Y. Peng, J. Zhu, W. Zhao and X. Liu, *Prog. Polym. Sci.*, 2021, **113**, 101353.
19 S. Stankovich, D. A. Dikin, G. H. Dommett, K. M. Kohlhaas, E. J. Zimney, E. A. Stach, R. D. Piner, S. T. Nguyen and R. S. Ruoff, *Nature*, 2006, **442**, 282–286.
20 J. C. Yoon, X. Dai, K. N. Kang, J. Hwang, M. J. Kwak, F. Ding and J. H. Jang, *ACS Nano*, 2021, **15**, 11655–11666.
21 A. C. Ferrari and D. M. Basko, *Nat. Nanotechnol.*, 2013, **8**, 235–246.
22 J. Lin, Z. Peng, Y. Liu, F. Ruiz-Zepeda, R. Ye, E. L. Samuel, M. J. Yacaman, B. I. Yakobson and J. M. Tour, *Nat. Commun.*, 2014, **5**, 5714.
23 D. X. Luong, K. V. Bets, W. A. Algozeeb, M. G. Stanford, C. Kittrell, W. Chen, R. V. Salvatierra, M. Ren, E. A. McHugh, P. A. Advincula, Z. Wang, M. Bhatt, H. Guo, V. Mancevski, R. Shahsavari, B. I. Yakobson and J. M. Tour, *Nature*, 2020, **577**, 647–651.
24 O. V. Yazyev and Y. P. Chen, *Nat. Nanotechnol.*, 2014, **9**, 755–767.
25 W. Yu, Y. Peng, L. Cao, W. Zhao and X. Liu, *Carbon*, 2021, **183**, 600–611.

26 H. Huang, X. Ming, Y. Wang, F. Guo, Y. Liu, Z. Xu, L. Peng and C. Gao, *Carbon*, 2021, **180**, 197–203.
27 H. D. Jang and J. Jeong, *Aerosol Sci. Technol.*, 1995, **23**, 553–560.
28 Y. Yao, Z. Huang, P. Xie, S. D. Lacey, R. J. Jacob, H. Xie, F. Chen, A. Nie, T. Pu, M. Rehwoldt, D. Yu, M. R. Zachariah, C. Wang, R. Shahbazian-Yassar, J. Li and L. Hu, *Science*, 2018, **359**, 1489–1494.
29 H. Sun, J. Zhu, D. Baumann, L. Peng, Y. Xu, I. Shakir, Y. Huang and X. Duan, *Nat. Rev. Mater.*, 2018, **4**, 45–60.
30 H. Guo, A. Zhang, H. Fu, H. Zong, F. Jin, K. Zhao and J. Liu, *Chem. Eng. J.*, 2023, **453**, 139633.
31 A. Zhang, Q. Zhang, H. Fu, H. Zong and H. Guo, *Small*, 2023, 202303911.
32 H. Fu, A. Zhang, H. Guo, H. Zong, F. Jin, K. Zhao and J. Liu, *J. Energy Storage*, 2022, **56**, 106056.
33 H. Fu, A. Zhang, F. Jin, H. Guo and J. Liu, *ACS Appl. Mater. Interfaces*, 2022, **14**, 16165–16177.
34 H. Fu, A. Zhang, H. Zong, F. Jin, H. Guo and J. Liu, *J. Colloid Interface Sci.*, 2023, **629**, 938–949.
35 J. Li, K. Liu, T. Ding, P. Yang, J. Duan and J. Zhou, *Nano Energy*, 2019, **58**, 797–802.
36 T. Wei, M. Kohring, H. B. Weber, F. Hauke and A. Hirsch, *Nat. Commun.*, 2021, **12**, 552.
37 D. D. Han, Z. D. Chen, J. C. Li, J. W. Mao, Z. Z. Jiao, W. Wang, W. Zhang, Y. L. Zhang and H. B. Sun, *ACS Appl. Mater. Interfaces*, 2020, **12**, 25435–25443.
38 H. Wang, S. Min, Q. Wang, D. Li, G. Casillas, C. Ma, Y. Li, Z. Liu, L. J. Li, J. Yuan, M. Antonietti and T. Wu, *ACS Nano*, 2017, **11**, 4358–4364.
39 Y. Shi, R. Li, Y. Jin, S. Zhuo, L. Shi, J. Chang, S. Hong, K.-C. Ng and P. Wang, *Joule*, 2018, **2**, 1171–1186.
40 E. L. Starostin and G. H. van der Heijden, *Nat. Mater.*, 2007, **6**, 563–567.
41 E. Garcia-Tunon, S. Barg, J. Franco, R. Bell, S. Eslava, E. D'Elia, R. C. Maher, F. Guitian and E. Saiz, *Adv. Mater.*, 2015, **27**, 1688–1693.
42 R. Ifuku, K. Nagashio, T. Nishimura and A. Toriumi, *Appl. Phys. Lett.*, 2013, **103**, 033514.

